

# Moments reconstruction and local dynamic range compression of high order Superresolution Optical Fluctuation Imaging

XIYU YI,<sup>1,\*</sup> SUNGHO SON,<sup>2</sup> RYOKO ANDO,<sup>3</sup> ATSUSHI MIYAWAKI,<sup>3</sup> AND SHIMON WEISS<sup>1,4,5,6,\*</sup>

<sup>1</sup>*Department of Chemistry and Biochemistry, University of California, Los Angeles, CA 90095, USA*

<sup>2</sup>*Department of Ecology and Evolutionary Biology, University of California, Los Angeles, CA 90095, USA*

<sup>3</sup>*Laboratory for Cell Function and Dynamics, RIKEN Center for Brain Science, Saitama 351-0198, Japan*

<sup>4</sup>*Department of Physiology, University of California, Los Angeles, CA 90095, USA*

<sup>5</sup>*California Nano Systems Institute, University of California, Los Angeles, CA 90095, USA*

<sup>6</sup>*Department of Physics, Institute for Nanotechnology and Advanced Materials, Bar-Ilan University, Ramat-Gan, 52900, Israel*

\*[xiyu.yi@gmail.com](mailto:xiyu.yi@gmail.com), \*[sweiss@chem.ucla.edu](mailto:sweiss@chem.ucla.edu)

**Abstract:** Super-resolution Optical Fluctuation Imaging (SOFI) offers a simple and affordable alternative to other super-resolution (SR) imaging techniques. The theoretical resolution enhancement of SOFI scales linearly with the cumulants' order, while imaging conditions are less phototoxic to living samples as compared to other SR methods. High order SOFI could, therefore, be a method of choice for dynamic live cell imaging. However, due to cusp-artifacts and to dynamic range expansion of pixel intensities, this promise has not been materialized as of yet. Here we investigated and compared high order moments vs. high order cumulants SOFI reconstructions. We demonstrate that even-order moments reconstructions are intrinsically free of cusp artifacts, allowing for a subsequent deconvolution operation to be performed, hence enhancing the resolution even further. High order moments reconstructions performance was examined for various (simulated) conditions and applied to (experimental) imaging of QD labeled microtubules in fixed cells, and actin stress fiber dynamics in live cells.

## 1. Introduction

Fluorescence microscopy is widely used in biological studies due to its high sensitivity and specificity, affording molecular-specific visualization of molecular structures and organelles in live cells in real-time. However, the spatial resolution of conventional fluorescence microscopy is limited by the Abbe's diffraction limit[1]. Advances in super-resolution (SR) imaging techniques, such as stimulated emission depletion (STED) microscopy[2], photo-activated localization microscopy (PALM)[3, 4], stochastic optical reconstruction microscopy (STORM)[5], structured illumination microscopy (SIM)[6] and their derivatives, allows us to overcome the diffraction limit and achieve optical resolution down to a few tens of nanometers[3, 7-10]. Such a dramatic resolution enhancement has already yielded significant discoveries[11-14]. A more recent addition to the SR toolbox is Super-resolution Optical Fluctuation Imaging (SOFI)[15]. SOFI is highly compatible with different imaging platforms, and has been demonstrated with wide-field microscopy (with either laser or Xenon lamp illumination)[16], total internal reflection fluorescence (TIRF) microscopy[17-21], multi-plane wide-field fluorescence microscopy[22], spinning-disk confocal microscopy[23], and light sheet microscopy[24]. The resolution enhancement of SOFI relies on the stochastic fluctuations of optical signals originating from the blinking emitters (see below), scatterers (as blinking Raman[25]), or absorbers[26]. Blinking fluorescence probes have been most commonly used in SOFI, including fluorescent proteins (FPs)[21, 27], organic dyes[28], quantum dots[15], and

carbon nanodots[19]. Other types of optical fluctuations have also been exploited for SOFI imaging, such as the ones originated from diffusion of probes[29], FRET due to diffusion[30], and stochastic speckle illumination [31].

Advantages of SOFI include compatibility with different imaging platforms and a wide variety of blinking probes, flexibility in imaging conditions[25], and a useful trade-off between spatial and temporal resolutions. Therefore, SOFI has the potential to democratized SR with a wide variety of applications

The theoretical resolution enhancement for SOFI is  $n^{1/2}$  fold for  $n$ th order cumulant[15]. Once combined with deconvolution or Fourier re-weighting, the enhancement becomes  $n$  fold[32]. Such resolution enhancement with the increase of SOFI order suggests that it would be beneficial to seek high SR performance using high order SOFI. In practice, however, two fundamental issues limit the application of high-order SOFI: (i) non-linear expansion of the dynamic range of pixel intensities[15] and (ii) cusp-artifacts[33]. Concerning issue (i), a partial solution for the dynamic-range expansion has been introduced as balanced-SOFI(bSOFI)[34]. Concerning issue (ii), cusp-artifacts are much harder to solve. In the original introduction of SOFI[15], cumulants were chosen over moments because the combinations of nonlinear cross-terms originated from multiple emitters are eliminated in cumulants. We recently found, however, that cumulants could yield mixture of positive and negative virtual brightnesses that lead to cusp-artifacts[33]. By averaging cumulants calculated from different time blocks, these artifacts could potentially be eliminated[36], but it requires prolonged data acquisition (with no drift) and applicable to static features only. Theoretically, another option to avoid/eliminate cusp artifacts would be to manipulate emitters' blinking behavior spatially, to yield a uniform sign for all cumulants across the image[33]. Such an option, however, is a challenging task, especially for live cell imaging where the labeling is often realized through the fusion of fluorescence proteins.

In this work, we examine the mathematically non-rigorous, but practical solution of high order SOFI using moments reconstruction. We show that even- and high-order moments reconstruction eliminates cusp artifacts while still providing SR enhancement. We also provide in-depth comparisons between cumulants and moments for various simulated and experimental conditions. We also made the associated datasets[37-39], simulation code package[40], and the data processing scripts[41] open to the public, as posted on the online repositories.

The outline of this manuscript is as follows: in **section 2** we briefly summarize SOFI theory and outline the relationship between correlation functions, cumulants, and moments. In **section 3**, we introduce the proposed moments reconstruction method and show that even-order moments are free of cusp artifacts. Moments reconstruction, however, introduces new artifacts due to nonlinear cross-terms. Based on the theoretical formulation, we interpret these cross-terms as the contribution from *ghost emitters* in the high order SOFI image. With both theory and simulations, we demonstrate that even-order moments yield a pure positive image, free of cusp artifacts, which is suitable for subsequent deconvolution operation. In **section 4** we introduce a new method that minimizes the ill-effects of expansion of the dynamic range of pixel intensities. We dub this method “local dynamic range compression” (*ldrc*). It locally compresses the dynamic range of pixel intensities, and its performance is not affected by cusp artifacts. This section also includes extensive simulations of various (and relevant) sample conditions that are subsequently analyzed by even-order moments reconstruction together with *ldrc*. In **Section 5** we present 6<sup>th</sup> order moment reconstructions for experimental data along with deconvolution and *ldrc*. The data sets include the quantum dot (QDs)-labeled microtubules in fixed cells and the fluorescence protein-labeled  $\beta$ -actin in live cells. Our results are then compared to results obtained by operating the bSOFI[34] and SRRF[42] algorithms to the same data sets. A concluding discussion is given in **section 6**, summarizing our main findings: (I) even-order moments reconstruction is intrinsically free of cusp artifacts; (II) it can be

independently combined with deconvolution without conflicting with the commonly used positivity constraint in image deconvolution; and (III) application of *ldrc* can correct for the expanded dynamic range of pixel intensities. These attributes allow for SR reconstruction of fast (~seconds) morphological changes in live cells.

## 2. Review of SOFI, correlations, cumulants, and moments

We briefly repeat here SOFI theory[15] but re-cast it in a form that affords the virtual emitter interpretation of SOFI at high orders[33]. This re-casting provides insight into high order SOFI cumulants and the proposed moments reconstruction. In the practice of SOFI, the sample is labeled with stochastically blinking emitters. This labeled sample is then imaged and consecutive frames are recorded. The data set is then SOFI processed to yield the SOFI image. Given a sample with  $N$  emitters that independently blink, the fluorescence signal captured at location  $\vec{r}$  and time  $t$  is given by:

$$F(\vec{r}, t) = \sum_{k=1}^N \epsilon_k \cdot b_k(t) \cdot U(\vec{r} - \vec{r}_k), \quad (2.1)$$

where  $k$  is the index of the emitter,  $\epsilon_k$  is the 'on'-state brightness of the  $k^{\text{th}}$  emitter,  $b_k(t)$  is the stochastic time dependent blinking profile of  $k^{\text{th}}$  emitter where:

$$b_k(t) = \begin{cases} 1 & \text{when the emitter is in the "on" state} \\ 0 & \text{when the emitter is in the "off" state} \end{cases} \quad (2.2)$$

$U(\vec{r})$  is the point-spread-function (PSF) of the imaging system, and  $\vec{r}_k$  is the location of the  $k^{\text{th}}$  emitter. In SOFI calculations, we first take the raw data with  $T$  total number of frames, and calculate the time-average of each pixel as follows:

$$\langle F(\vec{r}, t) \rangle_t = \frac{1}{T} \sum_{t=1}^T F(\vec{r}, t) \quad (2.3)$$

We subtract the time average  $\langle F(\vec{r}, t) \rangle_t$  from  $F(\vec{r}, t)$  to yield the temporal fluctuations  $\delta F(\vec{r}, t)$  of each pixel:

$$\delta F(\vec{r}, t) = F(\vec{r}, t) - \langle F(\vec{r}, t) \rangle_t \quad (2.4)$$

Substitution of (2.3) and (2.4) into (2.1) leads to an expanded expression of  $\delta F(\vec{r}, t)$ :

$$\delta F(\vec{r}, t) = \sum_{k=1}^N \epsilon_k \cdot \delta b_k(t) \cdot U(\vec{r} - \vec{r}_k) \quad (2.5)$$

Then, we calculate the  $n^{\text{th}}$ -order auto-correlations of  $\delta F(\vec{r}, t)$  along the time axis with time lags  $(\tau_1, \tau_2, \dots, \tau_n)$ :

$$G_n(\vec{r}, \tau_1, \tau_2, \dots, \tau_n) = \langle \delta F(\vec{r}, t + \tau_1) \cdot \delta F(\vec{r}, t + \tau_2) \cdots \delta F(\vec{r}, t + \tau_n) \rangle_t \quad (2.6)$$

It is common to set the first time lag  $\tau_1$  to 0. Cross-correlations using  $\delta F(\vec{r}, t)$  from different pixel locations (different  $\vec{r}$  values) can also be calculated:

$$G_n(\vec{r}_1, \vec{r}_2, \dots, \vec{r}_n; \tau_1, \tau_2, \dots, \tau_n) = \langle \delta F(\vec{r}_1, t + \tau_1) \cdot \delta F(\vec{r}_2, t + \tau_2) \cdots \delta F(\vec{r}_n, t + \tau_n) \rangle_t \quad (2.7)$$

By replacing  $\delta F(\vec{r}_i, \tau_i)$  with the notation  $\delta F_i$ , equation (2.7) can be simplified:

$$G_n(\delta F_1, \delta F_2, \dots, \delta F_n) = \langle \delta F_1 \cdot \delta F_2 \cdots \delta F_n \rangle_t \quad (2.8)$$

We address  $G_n(\delta F_1, \delta F_2, \dots, \delta F_n)$  as the joint correlation function for set  $\{\delta F_i | i \in [1, n]\}$ , which is defined by the chosen combinations of pixels and time lags. We also address  $G_n(\delta F_1, \delta F_2, \dots, \delta F_n)$  as the **joint-moment** of set  $\{\delta F_i | i \in [1, n]\}$ . The next step is to calculate the  $n^{\text{th}}$  order cumulant, denoted as  $C_n(\delta F_1, \delta F_2, \dots, \delta F_n)$ , which we address as the **joint-cumulant** of set  $\{\delta F_i | i \in [1, n]\}$ . Note that the special case of equation (2.7) with  $\vec{r} = \vec{r}_1 = \dots = \vec{r}_n$  reduces to equation (2.6), where the former addresses cross-correlation functions of signal traces from non-identical pixels, and the later addresses auto-correlation functions of signal trace from an identical pixel. Consequently, the differences between auto-correlation functions and cross-correlation functions are diminished while we form our discussion under the framework of joint-moments and joint-cumulants.

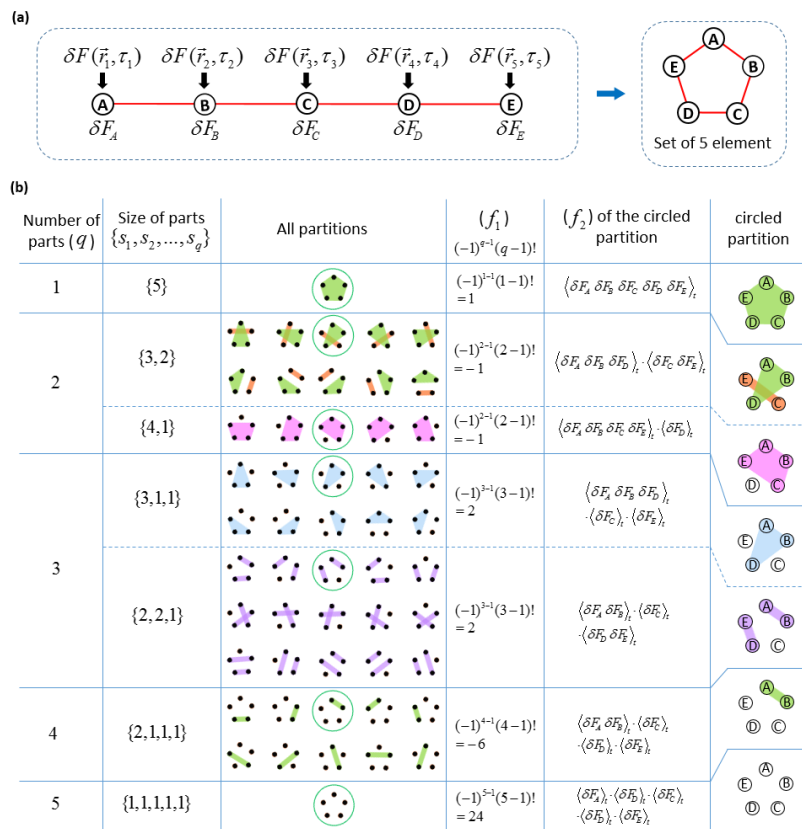


Fig. 1. Calculation of the 5<sup>th</sup> order joint-cumulants. A set of five elements is shown in (a), where the elements are the fluctuation profiles of five pixels. Duplication of pixels are allowed but not enforced. For example, if element A and B are duplicated pixels, we have  $\vec{r}_1 = \vec{r}_2$ . Simplified notations for the five elements are  $\{\delta F_A, \delta F_B, \delta F_C, \delta F_D, \delta F_E\}$  respectively. (b) demonstrates all possible partitions of the set of five elements, and how each partition contributes a term to the summation series (as the product of  $f_1$  and  $f_2$ ) to yield the joint-cumulant. Note that all the partitions that contain a part of size 1 are equal to 0, because  $\langle \delta F(t) \rangle_t = 0$ . The graphical demonstration of partitions is inspired by the work by Tilman Piesk [1].

The calculation of the joint-cumulant of set  $\{\delta F_i | i \in [1, n]\}$  is illustrated in (2.9), using the case of 5<sup>th</sup> order as an example. In the general sense, regardless of the choices of  $\{\delta F_i | i \in [1, n]\}$ ,  $n$  fluorescence fluctuations profiles are selected from individual pixels (with

or without duplicated pixels) to form the set  $\{\delta F_i | i \in [1, n]\}$  (Fig. 1 (a)), from which all the possible partitions are identified as shown in Fig. 1(b). Partitions possess different numbers of parts where each part possess a certain numbers of elements (1<sup>st</sup> and 2<sup>nd</sup> columns in Fig. 1(b)). For each partition, the elements of set  $\{\delta F_i | i \in [1, n]\}$  are grouped into specific parts, where each part is a subset of  $\{\delta F_i | i \in [1, n]\}$  (3<sup>rd</sup> column in Fig. 1(b)). Each specific partition of set  $\{\delta F_i | i \in [1, n]\}$  contributes a term to a summation series to construct the joint-cumulant, where each term can be expressed as the product of two factors. This is shown in the 4<sup>th</sup> and 5<sup>th</sup> column in Fig. 1(b). The first factor  $f_1$  depends on the size of this partition (denoted as  $q$  in 1<sup>st</sup> column in Fig. 1(b)) and is defined as:  $f_1 = (-1)^{q-1} (q-1)!$  (4<sup>th</sup> column in Fig. 1(b)). The second factor  $f_2$  is the product of all the joint-moments of each part within this partition, as illustrated in the 5<sup>th</sup> column in Fig. 1(b): if we use  $I$  to represent set  $\{\delta F_i | i \in [1, n]\}$  and  $I_p$  (with  $p=1,2,3,\dots,q$ ) to represent different parts that belong to this partition (as different subsets of  $I$ ), we have  $I_1 \cup I_2 \cup \dots \cup I_q = I$ . The joint-moments for each part  $I_p$  (denote as  $G(I_p)$ ) are multiplied together to yield  $G(I_1) \cdot G(I_2) \cdots G(I_q)$  as the second factor ( $f_2$ ).

In conclusion, given a set of intensity trajectories from a group of pixels (set  $I$ ) (either with or without duplicated pixels), the joint-cumulant of  $I$  is constructed as a function of the joint-moments of all parts over all possible partitions of set  $I$ , based on the following formula[43]:

$$C_n(I) = \sum_{\substack{I_1 \cup I_2 \cup \dots \cup I_q \\ = \{\delta F_i | i \in [1, n]\} \\ \text{all partitions of} \\ \text{set } \{\delta F_i | i \in [1, n]\}}} (-1)^{q-1} (q-1)! G(I_1) \cdot G(I_2) \cdots G(I_q) \quad (2.9)$$

Note here that in equation (2.9), the joint-moments  $G(I_p)$  are essentially the lower order correlation functions discussed in the original work of SOFI [15]. If a partition contains a part that has only one element, we have the corresponding  $G(I_p)$  as  $\langle \delta F(t) \rangle_t = 0$ . As a result, the corresponding  $f_2$  factor will be 0, and this partition will not contribute to the joint-cumulant. The calculation of  $C_5(I)$  is shown in Fig. S1[47] as an example.

By substituting equation (2.1) - (2.8) into equation (2.9), the  $n^{\text{th}}$  order joint-cumulant of set  $\{\delta F_i | i \in [1, n]\}$  can be expressed as follows:

$$\begin{aligned} & C_n(\vec{r}_1, \vec{r}_2, \dots, \vec{r}_n; \tau_1, \tau_2, \dots, \tau_n) \\ &= W_n(\vec{r}_1, \vec{r}_2, \dots, \vec{r}_n) \cdot \sum_{k=1}^n \epsilon_k^n C_n(\delta b_k(t + \tau_1), \delta b_k(t + \tau_2), \dots, \delta b_k(t + \tau_n)) \cdot U^n(\vec{r}_{gc} - \vec{r}_k) \\ & \quad \text{with:} \\ & W(\vec{r}_1, \vec{r}_2, \dots, \vec{r}_n) = \prod_{\substack{i < j \\ i \in [1, n] \\ j \in [1, n]}} U\left(\frac{\vec{r}_i - \vec{r}_j}{\sqrt{n}}\right) \quad ; \quad \vec{r}_{gc} = \frac{1}{n}(\vec{r}_1 + \vec{r}_2 + \dots + \vec{r}_n) \end{aligned} \quad (2.10)$$

where  $W_n(\vec{r}_1, \dots, \vec{r}_n)$  is the distance factor[15]. The PSF can be approximated by a Gaussian function:

$$U(\vec{r}) = \exp\left(-\frac{r_x^2 + r_y^2}{2\omega_{xy}^2} - \frac{r_z^2}{2\omega_z^2}\right) . \quad (2.11)$$

Detailed derivation of equation (2.10) can be found in Appendix 1[47]. Once the distance factor is solved and divided from both sides of equation (2.10), the cumulant value at location  $\vec{r}_{gc}$  is obtained.

The vector that describes the location of a SOFI pixel is equivalent to the average of the vectors that describe the locations of all the selected pixels. In the case when duplication of pixels exists, the corresponding location vectors are duplicated as well. The choice of pixel combination imposes a trade-off between noise contribution and the attenuation of cumulant

value imposed by the distance factor  $W_n(\bar{r}_1, \dots, \bar{r}_n)$  (defined in (2.10)). On one hand, noise could potentially contribute to the resultant cumulant value if there is pixel duplication in the selection. On the other hand, when the selected pixels are distributed too far away from each other, the distance factor becomes small and attenuates the recovered pixel value. Existing approaches have been focused on avoiding the noise contribution from duplicated pixels[44], but here we explore and present the opposite of this trade-off, where we want to diminish the effect of the distance factor at the cost of potential noise contribution. A detailed explanation for our choice of pixel combinations for high order SOFI is given in Appendix 2[47] and Fig. S2[47].

Under the framework of virtual emitter interpretation[33], the physical meaning of the joint-cumulant calculated for a set of pixels (with or without duplicated pixels) is as follows: The image of the cumulants is as formed by virtual emitters at the locations of the original emitters, but having virtual brightnesses. These virtual brightnesses are the products of  $\epsilon^n$  (meaning the  $n^{\text{th}}$  power of the original ‘on-state’ brightness of the emitter) and  $w_n(\delta b_k(t))$  (meaning the  $n^{\text{th}}$  order cumulant of the blinking profile of the  $k^{\text{th}}$  emitter). Considering that the blinking statistics of emitters across the image are not necessarily spatially uniform, especially in the case of live-cell imaging with fluorescence protein fusion. The ‘on-time ratio’, defined as the percentage of time the emitter spent at ‘on’ state, can vary, causing cumulant values to have different signs at different parts of the image (Fig. 2). Since images are usually presented with positive pixel values, taking the absolute value could yield an image with cusp-artifacts, degrading the image quality of high-order SOFI cumulants[33]. Furthermore, the cusp-artifacts limit the subsequent deconvolution process because the absolute value of the image is no longer a convolution process, while the original image carries negative values that conflict with the commonly used positivity constraint in deconvolution algorithms.

### 3. High-order moments reconstruction – theory and Interpretation

Inspired by the interchangeable relation between cumulants and moments[35], we investigated the statistical behavior of high-order moments of emitter blinking trajectories expressed as a function of the ‘on time ratio’ in a similar way to cumulant analysis[33]:

$$M_n(\rho) = (1-\rho)^n \cdot \rho + (-\rho)^n \cdot (1-\rho) \quad (3.1)$$

Fig. 2 shows the comparisons of moments (Fig. 2(a)) and cumulants (Fig. 2(b)) of different orders as a function of  $\rho$ . While cumulants exhibit oscillation between positive and negative values, even-order moments have pure positive values (and odd-order moments are bi-modal and have a single node).

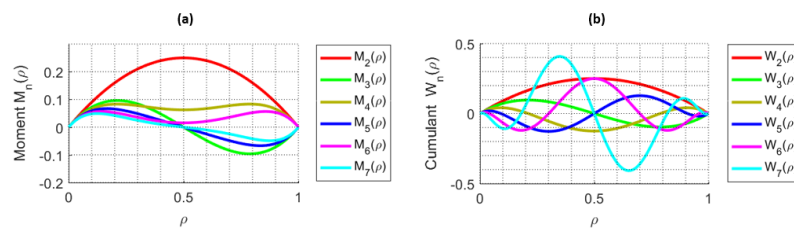


Fig. 2. Moments and cumulants as a function of the ‘on time ratio’  $\rho$ . (a) shows different moments as a function of  $\rho$  and denoted as  $M_n(\rho)$ , and (b) shows different cumulants as a function of  $\rho$  and denoted as  $W_n(\rho)$ . In both notations,  $n$  represents the order.

In practice, blinking behavior of fluorophores are not well controlled, therefore, can be composed of mixtures of positive and negative virtual brightnesses[33], leading to cusp artifacts[33]. Since even-order moments are always positive, therefore, eliminate cusp artifacts, we decided to examine their ability and fidelity in reconstructing SR images of the high orders.

As explained in the introduction, we note here that such a reconstruction is mathematically non-rigorous due to nonlinear cross-terms containing mixed signals from multiple emitters. Our examination could, however, evaluate the benefits of eliminating cusp artifacts vs. the drawbacks of introducing additional virtual emitters (originated from cross-terms). Moreover, since even-order moments reconstruction contains pure sign (purely positive), and the absolute-value image is free of cusp artifacts, subsequent deconvolution operation (that often carries positivity constraint) could further enhance the resolution.

In order to better understand the physical meaning of moments, we look at the form of moments derived from cumulants according to Kendall et al[35]:

$$M_n(\vec{r}; \tau = 0) = \sum_{\substack{I_1 \cup I_2 \cup \dots \cup I_\sigma \\ = \{\delta F_i | i \in [1, n]\} \\ \text{all partitions of} \\ \text{set } \{\delta F_i | i \in [1, n]\}}} C_{s_1}(\vec{r}, \tau = 0) \cdots C_{s_\sigma}(\vec{r}, \tau = 0) \quad (3.2)$$

where  $\{I_p | p \in [1, \sigma]\}$  is one partition of set  $\{\delta F_i | i \in [1, n]\}$ ,  $\sigma$  is the size of this partition (i.e. the total number of parts within this partition),  $S_p$  is the size of  $I_p$ , and  $C_{s_p}(\vec{r}, \tau = 0)$  is the  $S_p^{\text{th}}$  order cumulant of fluorescence fluctuation at location  $\vec{r}$  with all the time lags equal to 0. Note here that we use  $\sigma$  (instead of  $q$ ) to represent the size of the partition to distinguish moments reconstruction from cumulants reconstruction. The reconstruction algorithm is shown in the flow diagram of Fig. S3.[47]. With the goal of achieving  $n^{\text{th}}$  order moments reconstruction, we can interpolate all calculated cumulants (2<sup>nd</sup> order to  $n^{\text{th}}$  order) onto a unified high resolution spatial grid that supports all orders. This re-mapping provides a full set of cumulants for each pixel if we need interpolation. Next, different orders of cumulants are combined (as shown in equation (3.2)) to reconstruct the moments at each pixel. A similar re-mapping could be achieved using fSOFI[45] with interpolation performed on each frame of the acquired image, followed by correlation calculations to directly compute the moments. When all the time lags used in the correlation calculation are zero, the computational cost for the moments computation at each interpolated pixel is greatly reduced. The analytical expression for reconstructed moments is:

$$\begin{aligned} M_n(\vec{r}; \tau = 0) &= \sum_{\substack{I_1 \cup I_2 \cup \dots \cup I_\sigma \\ = \{1, 2, \dots, n\} \\ \text{all partitions of} \\ \text{set } \{1, 2, \dots, n\}}} C_{s_1}(\vec{r}, \tau = 0) \cdots C_{s_\sigma}(\vec{r}, \tau = 0) \\ &= \sum_{\substack{I_1 \cup I_2 \cup \dots \cup I_\sigma \\ = \{1, 2, \dots, n\} \\ \text{all partitions of} \\ \text{set } \{1, 2, \dots, n\}}} \left[ \sum_{k_1=1}^N \cdots \sum_{k_\sigma=1}^N \left( \prod_{p=1}^{\sigma} \epsilon_{k_p}^{s_p} \right) \left( \prod_{p=1}^{\sigma} C_{s_p}(\delta b_{k_p}(t)) \right) U^n(\vec{r} - \vec{r}_m) W(\{s_p, \vec{r}_{k_p}\}) \right] \end{aligned} \quad (3.3)$$

where  $W$  is the ‘emitter distance factor’, whose analytical form is the same with that of the distance factor[15] that is dependent on the mutual distances between different pixels (instead of different emitters here) as shown in (2.10). Detailed derivations of equation (3.3) is given in Appendix 3[47]. We also define  $\vec{r}_m$  as:

$$\vec{r}_m = \frac{1}{n} \sum_{p=1}^{\sigma} S_p \cdot \vec{r}_{k_p} \quad (3.4)$$

to be the mass center of the mass points (indexed with  $p$  as shown in (3.4)) at locations  $\vec{r}_{k_p}$  (index  $k_p$  is defined in (3.3)) with mass values  $S_p$ . Therefore, we can re-index the summation series of equation (3.3) into the summation over all possible mass centers. Consequently, the moments reconstruction is formed as the convolution between a virtual PSF ( $U^n(\vec{r})$ ) and a virtual ground truth location map constitutes of all the mass centers. The virtual PSF is the

original PSF raised to the power of  $n$  that maintains the theoretical resolution enhancement, and the virtual ground truth location map is described by the superposition of virtual emitters with locations described by (3.4). To gain more intuitive insight, the summation series in equation (3.3) can be divided into two parts. The first part is the case when all the emitter vectors in (3.4) are identical, they describe the virtual emitter that is located at the original real emitter location. As shown below:

$$M1_n(\vec{r}; \tau = 0) = \sum_{\substack{I_1 \cup I_2 \cup \dots \cup I_n \\ = \{1, 2, \dots, n\} \\ \text{all partitions of} \\ \text{set } \{1, 2, \dots, n\}}} \left[ \sum_{k=1}^N \left( \prod_{p=1}^{\sigma} \epsilon_k^{s_p} \right) \left( \prod_{p=1}^{\sigma} C_{s_p}(\delta b_k(t)) \right) U^n(\vec{r} - \vec{r}_m) \right] \quad (3.5)$$

$M1_n$  is the part with identical location vectors representing real emitters at locations  $\vec{r}_k$ . The equation can be simplified into the following form (as shown in Appendix 8[47]):

$$M1_n(\vec{r}; \tau = 0) = \sum_{k=1}^N \epsilon_k^n U^n(\vec{r} - \vec{r}_m) M_n(\delta b_k(t)) \quad (3.6)$$

From equation (3.6) we deduce that this portion of the signal ( $M1_n$ ) is equivalent to an image formed by virtual emitters located at the same locations as the original emitters but with changed brightnesses  $\epsilon_k^n M_n(\delta b_k(t))$  (for the  $k^{\text{th}}$  virtual emitter). These brightnesses differ from the ones derived for cumulants[33]:  $\epsilon_k^n C_n(\delta b_k(t))$ . For the  $k^{\text{th}}$  virtual emitter, its virtual brightness is the product between the  $n^{\text{th}}$  power of its on-state brightness  $\epsilon_k^n$  multiplied by the  $n^{\text{th}}$  order moment (instead of cumulant) of its blinking fluctuation  $\delta b_k(t)$ . Because  $\epsilon_k^n$  is always positive, even order moments are always positive. Therefore the virtual brightness for this portion of the moments signal is always positive.

The second, non-physical part of the summation series in equation (3.3) is the case where the partitions contain non-identical emitter location vectors. The corresponding virtual emitters are located at locations where there are no real emitters (unless by coincidence the mass center overlaps with the location of a real emitter). It originates from cross-terms of signals coming from non-identical emitters. They take the form of virtual emitters at new locations and dubbed here as ‘ghost’-emitters. The brightnesses of these ‘ghost’-emitters are attenuated by the emitter distance factor, ranging from 0 to 1 as represented in the same analytical form of the original distance factor[15].

#### 4. High-order moments reconstruction of simulated data

To take a close look of the resolution enhancement and assess the contribution of ‘ghost’-emitters, we simulated 3 near-by Poisson-blinking fluorophores and reconstructed the moments of the simulated movie (Fig. 3). The parameters used to generate the blinking trajectories are tabulated in Fig. 3(a), and the positions of the 3 emitters are shown in Fig. 3(b). Fig. 3(c) compares 6<sup>th</sup> order moments-reconstruction of the simulated movie with the prediction (calculated from equation (3.3)) using the ground truth of blinking parameters used in the simulation). The resolution enhancement mechanism is also confirmed in Fig. 3(d) with increasing order of moments and decreasing size of the PSFs of the three emitters. We note that the prediction is affected by the time-binning introduced by the camera’s frame integration time. A correction for the binning effect could be introduced to the theoretical framework as was done by Kendall et al.[35]. (but this is beyond the scope of the work presented here).



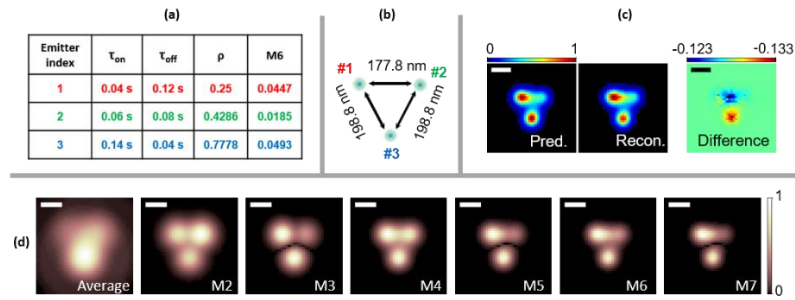


Fig. 3. Moments reconstruction of simulated data for 3 near-by blinking fluorophores. (a) shows the photophysical parameters used in the blinking simulation of the three emitters. (b) shows the ground truth location of the three emitters. Other parameters used for the simulations: emission wavelength of 520nm, numerical aperture of  $NA=1.4$ , frame integration time of 2 ms. The pixel size was set to be small (17.78 nm) to avoid artifacts due to binning. (c) shows the comparison between the prediction (Pred.) and reconstruction (Recon.) of the 6<sup>th</sup> order moment. (d) shows the average image (Ave.) and moments of the simulated movie (M2 to M7). Scale bars: 160 nm.

Because the emitter distance factor  $W(s_p, r_k)$  attenuates the virtual brightnesses of the ghost emitters (see Fig. S5[47]), their contribution to the image is to ‘fill-in’ the space in between the real emitters #1, #2 and #3. Nonetheless, despite this smoothing-out effect, SR enhancement is still maintained (Fig. S4[47]). Importantly, even order moments are free of cusp-artifacts (see Fig. S5[47]). As distances between emitters increase, ghost emitters’ intensities are further attenuated (Fig. S5[47]). We compared the performance of the 6<sup>th</sup> order moments reconstruction to the value of the 3<sup>rd</sup> power of 2<sup>nd</sup> order cumulant, and have shown that moments reconstructions have more assessable artifacts. Consequently, the artifacts introduced by ‘ghost’ emitters in moments is a manageable imperfection (Fig. S6[47]). Even-order moments reconstruction is free of cusp artifact (virtual and real brightnesses are positive), and the ghost emitters’ artifact is limited due to brightness attenuation.

Considering the existence of ghost emitters, the lower limit of the resolution enhancement of  $n^{\text{th}}$  order moments reconstruction (where  $n$  is an even number) is the resolution enhancement acquired in the 2<sup>nd</sup> order moment (equivalent to the 2<sup>nd</sup> order cumulant in our case):  $\sqrt{2}$ . However, because of its immunity to cusp-artifacts, deconvolution algorithms could be readily applied to further enhance the resolution by up to an addition of  $n^{1/2}$  fold[32], resulting in a factor of  $\sqrt{2n}$  resolution enhancement. This resolution enhancement factor is higher than that for pure cumulants without deconvolution ( $n^{1/2}$ ), but lower than for cumulants with deconvolution ( $n$ ). However, cusp-artifacts greatly corrupt high-order cumulants, rendering deconvolution impractical. A similar argument holds for bSOFI reconstruction which assumes perfect deconvolution.

We further increased the complexity of the simulations for various sample conditions and assessed the performance of the 6<sup>th</sup> order moments reconstructions in comparison to the performance of bSOFI and SRRF reconstructions for the same data sets. The moment reconstruction was combined with a cusp-independent dynamic range compression method *ldrc* that we designed (see Appendix 4[47]). All reconstructions were compared to the ground truth image. As shown in Fig. 4, bSOFI reconstruction exhibits discontinuities in the simulated filaments while SRRF artificially narrows them down. moments reconstructions yield a more faithful representation of the simulated data.

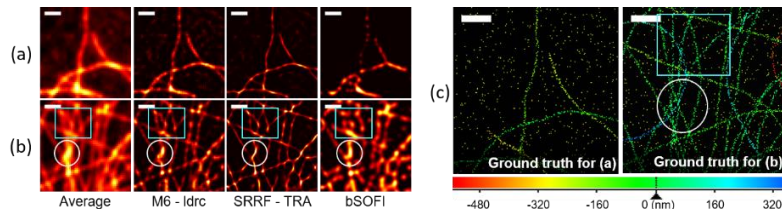


Fig. 4. Comparison of high-order moments reconstruction with high-order bSOFI and SRRF reconstructions on simulated filaments. A simulated dataset consisting of filaments in a 3D space was generated with: 50 emitters per 1  $\mu\text{m}$  labeling density along the line, 10 nm cross-section thickness with a Gaussian profile, 520 nm emission wavelength, 1.4NA and 90x magnification and a grid of  $125 \times 125$  pixels with a pixel size of  $1.6 \times 1.6 \mu\text{m}^2$ . The Gibson Lanni's PSF model was used in the simulations. Small field of views are cropped with different feature densities for comparison. (a) Sparse filaments. All methods yield satisfactory results. While M6-ldrc exhibits some grids artifacts, SRRF emphasizes thin features with oscillatory intensities and bSOFI exhibits granular and discontinuous features. (b) Dense filaments. Compared to the ground truth image, M6-ldrc exhibits the most faithful representation, while SRRF-TRA omits filaments (circled area for example). bSOFI exhibits discontinues filaments and features at locations that have no ground-truth signal (boxed area for example). (c) and (d) shows the ground truth for (a) and (b) as labeled in the image respectively. Scale bars: 640 nm.

Further results for a variety of simulated challenging image conditions are summarized in the Appendix[47], including for different labeling density (Fig. S8[47]), increased filaments thickness (or equivalently labeling uncertainty) (Fig. S9[47]), increased nonspecific binding emitter density (Fig. S10[47]), and various signal levels (Fig. S11[47]).

Details of the simulations are given in Appendix 5[47]. We further tested the 3D sectioning capability on an additional set of simulations where acquisitions of the same simulated sample at 100 different focal planes were generated[37] and processed independently and subsequently combined for 3D reconstruction. *ldrc* together with moments reconstruction have yielded better sectioning performance than SRRF when compared to the ground truth of the simulation (Fig. 5, Visualization 1, and Visualization 2).

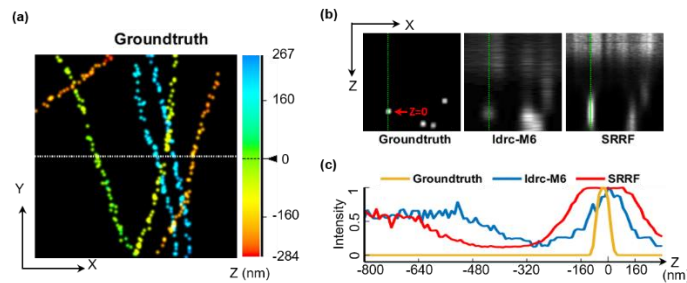


Fig. 5. Comparison of high-order moments reconstruction with high-order SRRF reconstruction for 3D sectioning performance. 3D sectioning results of ldrc-M6 and SRRF on simulated data are shown for a small field-of-view ( $2.15 \mu\text{m} \times 2.15 \mu\text{m}$ ). The full field-of-view results during a continuous scan of the focal plane is provided in SI Movie 1. (a) shows the ground truth image of the simulated filaments projected onto x-y plane. Emitters are represented by 3D delta functions convolved with a 3D Gaussian with FWHM = 86.27 nm for the purpose of display. The color scale represents the z coordinate of the emitters. (b) x-z scan corresponding to the dashed line in (a), where 4 filaments are penetrating through the plane (a fifth filament (yellow) is missing at this plane because the sparse, stochastic labeling algorithm did not place an emitter at the corresponding (x, y, z) coordinate). (c) A z-direction cross section of the first (green) filament for ground-truth and ldrc-M6 and SRRF reconstructions.

## 5. High-order moments reconstruction of experimental data

High-order moments reconstruction (6<sup>th</sup> order) in combination with *ldrc* and deconvolution were applied to experimental data of quantum dots-labeled  $\alpha$ -tubulin filaments in fixed HeLa cells. The results are compared to bSOFI and SRRF results (Fig. 6). As shown already in the previous section, SRRF exhibit the highest visual resolution enhancement, but at the expense of introduction of distortions, while *ldrc*-M6 exhibits more faithful results (as compared to the average image).

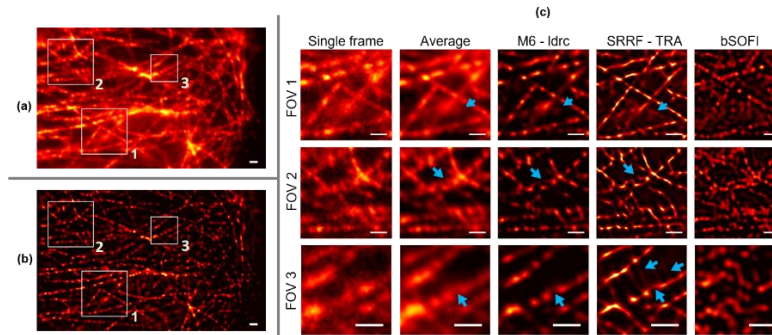


Fig. 6. High-order moments reconstruction of experimental data (fixed cells).  $\alpha$ -tubulin filaments in fixed HeLa cells were labeled with QD800. 1000 frames were acquired with 30 ms integration per frame and processed. (a) shows the average image (b) shows the *ldrc*-M6 results from the full field-of-view. Three zoom-in panels in (a) are shown in panel (c) as FOV1, FOV2 and FOV3 respectively, for single frame, average image, and results from *ldrc*-M6, SRRF and bSOFI respectively. bSOFI exhibit discontinuities, SRRF provides higher resolution details but with distortions (blue arrows). The *ldrc*-M6 image is similar to the average image but with less background and improved resolution. Scale bars: 800 nm.

*ldrc*-M6 results for live cell imaging[38] are shown in Fig. 7. Fluorescence labeling was performed by fusing  $\beta$ -Actin protein sequence to either Skylan-S[21] or Dronpa-C12 (Appendix 6[47], R. A. et al., manuscript in preparation) with a (GGGGS) $\times$ 3 linker. The bSOFI algorithm does not perform particularly well for this frame rate (33 Hz). SRRF, on the other hand, exhibits excellent performance regarding resolution enhancement and highlighting and preserving small features (green arrows), but at the cost of introducing extra features that could be artifacts (blue arrows). Besides, M6 results afford deconvolution post processing (DeconvSK[46]), while deconvolution performed on SRRF results highlights the artifacts. The reproducibility of the reconstruction algorithms and their comparisons could be assessed from reconstructions of additional experimental data sets (Fig. S12, S12, S13, S14[47] and Visualizations 3 - 8). Details of the experiments can be found in Appendix 6[47], and details of data processing can be found in Appendix 7[47]. Both SRRF and Moments reconstruction (M6+*ldrc*+deconvolution) outperform bSOFI and SOFI cumulants, especially when applied to fast live cell imaging data.

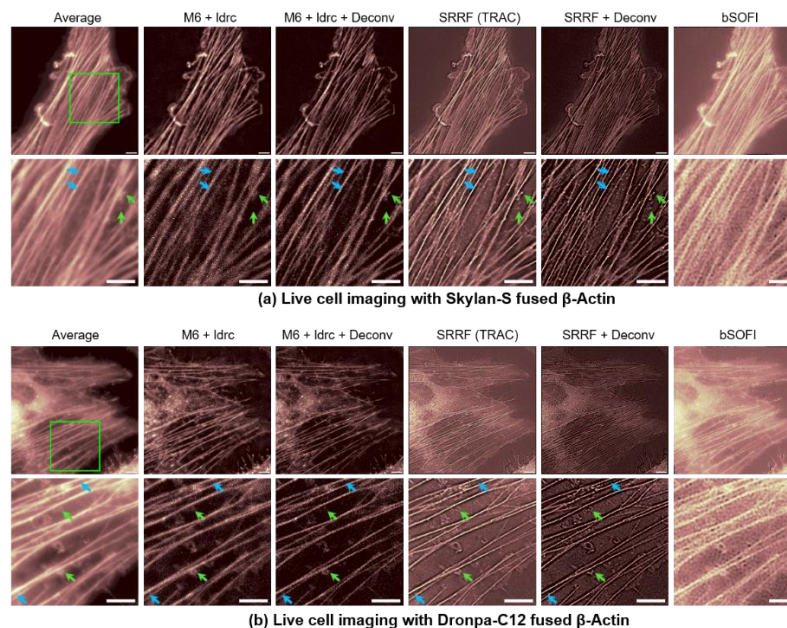


Fig. 7. High-order moments reconstruction of experimental data (live cells). HeLa cells were transfected with plasmid encoding (a) Skylan-S fused to  $\beta$ -Actin and (b) Dronpa-C12 fused to  $\beta$ -Actin. Live cells were imaged with 30 ms frame integration. 200 frames of the movie were processed per block. For each panel, top row shows the full field-of-view and the bottom row shows a zoom-in region (green box in the Average image). Each column shows results for the reconstruction method labeled at the top. Scale bars: 8  $\mu$ m. We can see that while SRRF exhibit excellent performance on highlighting small features (green arrows), but at the cost of introducing extra feature that could be artifacts (blue arrows).

## 6. Conclusions

As explained in our accompanying work[33], cusp artifacts significantly affect the quality of high-order SOFI (cumulant) reconstruction. In this paper, we reexamined the moments reconstruction and compared its results with cumulants, SRRF and bSOFI reconstructions. Although being mathematically non-rigorous, moments reconstructions (combined with *ldrc* and deconvolution) of simulated and experimental data sets exhibited satisfactory results with resolution enhancement and minimal distortions. Although they inherently introduce additional, spurious signals from virtual emitters, in practice, the reconstructions are faithful to the ground-truth of simulated data and average image of experimental data. Moments reconstruction and SRRF both outperform bSOFI due to the latter's heavy reliance on deconvolution. In contrast to bSOFI, Moments reconstruction allows for subsequently deconvolution algorithm to be applied to the reconstruction, independent of the dynamic range compression process. Lastly, we have demonstrated a super-resolved M6-reconstructed live cell movie with a temporal resolution of 6 seconds per frame (requiring only 200 frames of the original movie for each frame of the reconstructed movie) using a conventional wide-field fluorescence microscope.

## Funding

The work from Shimon Weiss and Xiyu Yi was supported by NSF STROBE: A National Science Foundation Science & Technology Center under Grant No. DMR 1548924 and by Dean Willard Chair funds. Sungho Son was supported by Raymond and Dorothy Wilson

Summer Research Fellowship. The work from Atsushi Miyawaki and Ryoko Ando was supported by grants from the Japan Ministry of Education, Culture, Sports, Science, and Technology Grant-in-Aid for Scientific Research on Innovative Areas: Resonance Bio, and the Brain Mapping by Integrated Neurotechnologies for Disease Studies (Brain/MINDS), and Japan Agency for Medical Research and Development-Core Research for Evolutional Science and Technology (AMED-CREST).

### Author contributions

S. W. and X. Y. designed the research, X. Y. and S. S. performed the experiments, X. Y. developed simulations, the analysis methods and the associated codes, R. A. and A. M. designed and developed the Dronpa-C12 protein. S. W. and X. Y. wrote the manuscript. These authors declare no conflict of interests.

### Acknowledgement

We would like to thank Prof. Pingyong Xu for providing the Skylan-S plasmid. We would like to thank Yingyi Lin and Xi Lin for their help with live-cell experiments.

### Disclosures

The authors declare that there are no conflicts of interest related to this article.

### References

1. E. Abbe, "VII.—On the Estimation of Aperture in the Microscope," *Journal of the Royal Microscopical Society* **1**, 388-423 (1881).
2. S. W. Hell and J. Wichmann, "Breaking the diffraction resolution limit by stimulated emission: stimulated-emission-depletion fluorescence microscopy," *Optics Letters* **19**, 780-782 (1994).
3. E. Betzig, G. H. Patterson, R. Sougrat, O. W. Lindwasser, S. Olenych, J. S. Bonifacino, M. W. Davidson, J. Lippincott-Schwartz, and H. F. Hess, "Imaging intracellular fluorescent proteins at nanometer resolution," *Science* **313**, 1642-1645 (2006).
4. E. Betzig, "Proposed Method for Molecular Optical Imaging," *Optics Letters* **20**, 237-239 (1995).
5. M. J. Rust, M. Bates, and X. W. Zhuang, "Sub-diffraction-limit imaging by stochastic optical reconstruction microscopy (STORM)," *Nature Methods* **3**, 793-795 (2006).
6. M. G. L. Gustafsson, "Surpassing the lateral resolution limit by a factor of two using structured illumination microscopy," *Journal of Microscopy-Oxford* **198**, 82-87 (2000).
7. A. Dani, B. Huang, J. Bergan, C. Dulac, and X. Zhuang, "Superresolution imaging of chemical synapses in the brain," *Neuron* **68**, 843-856 (2010).
8. Y. Doksani, J. Y. Wu, T. de Lange, and X. Zhuang, "Super-resolution fluorescence imaging of telomeres reveals TRF2-dependent T-loop formation," *Cell* **155**, 345-356 (2013).
9. K. Xu, G. Zhong, and X. Zhuang, "Actin, spectrin, and associated proteins form a periodic cytoskeletal structure in axons," *Science* **339**, 452-456 (2013).
10. B. J. Bellevue, A. N. Boettiger, M. S. Avendaño, R. Jungmann, R. B. McCole, E. F. Joyce, C. Kim-Kiselak, F. Bantignies, C. Y. Fonseka, and J. Erceg, "Single-molecule super-resolution imaging of chromosomes and in situ haplotype visualization using Oligopaint FISH probes," *Nature communications* **6**(2015).
11. M. Wojcik, S. Kohler, A. F. Demburg, and K. Xu, "Super-resolution microscopy reveals the three-dimensional organization of meiotic chromosome axes in intact *C. elegans* tissue," *Molecular Biology of the Cell* **27**(2016).
12. B. R. Han, R. B. Zhou, C. L. Xia, and X. W. Zhuang, "Structural organization of the actin-spectrin-based membrane skeleton in dendrites and soma of neurons," *Proceedings of the National Academy of Sciences of the United States of America* **114**, E6678-E6685 (2017).
13. K. Xu, G. S. Zhong, and X. W. Zhuang, "Actin, Spectrin, and Associated Proteins Form a Periodic Cytoskeletal Structure in Axons," *Science* **339**, 452-456 (2013).
14. A. N. Boettiger, B. Bintu, J. R. Moffitt, S. Y. Wang, B. J. Bellevue, G. Fudenberg, M. Imakaev, L. A. Mirny, C. T. Wu, and X. W. Zhuang, "Super-resolution imaging reveals distinct chromatin folding for different epigenetic states," *Nature* **529**, 418-+ (2016).
15. T. Dertinger, R. Colyer, G. Iyer, S. Weiss, and J. Enderlein, "Fast, background-free, 3D super-resolution optical fluctuation imaging (SOFI)," *Proceedings of the National Academy of Sciences of the United States of America* **106**, 22287-22292 (2009).
16. T. Dertinger, J. Xu, O. F. Naini, R. Vogel, and S. Weiss, "SOFI-based 3D superresolution sectioning with a widefield microscope," *Optical nanoscopy* **1**, 2 (2012).
17. E. Ambrose, "A surface contact microscope for the study of cell movements," *Nature* **178**, 1194-1194 (1956).
18. D. Axelrod, "Cell-Substrate Contacts Illuminated by Total Internal-Reflection Fluorescence," *Journal of Cell Biology* **89**, 141-145 (1981).

19. A. M. Chizhik, S. Stein, M. O. Dekaliuk, C. Battle, W. Li, A. Huss, M. Platen, I. A. Schaap, I. Gregor, and A. P. Demchenko, "Super-resolution optical fluctuation bio-imaging with dual-color carbon nanodots," *Nano letters* **16**, 237-242 (2015).
20. S. Geissbuehler, C. Dellagiocoma, and T. Lasser, "Comparison between SOFI and STORM," *Biomedical optics express* **2**, 408-420 (2011).
21. X. Zhang, X. Chen, Z. Zeng, M. Zhang, Y. Sun, P. Xi, J. Peng, and P. Xu, "Development of a reversibly switchable fluorescent protein for super-resolution optical fluctuation imaging (SOFI)," *ACS nano* **9**, 2659-2667 (2015).
22. S. Geissbuehler, A. Sharipov, A. Godinat, N. L. Bocchio, P. A. Sandoz, A. Huss, N. A. Jensen, S. Jakobs, J. Enderlein, and F. G. Van Der Goot, "Live-cell multiplane three-dimensional super-resolution optical fluctuation imaging," *Nature communications* **5**(2014).
23. X. Chen, Z. Zeng, H. Wang, and P. Xi, "Three-dimensional multimodal sub-diffraction imaging with spinning-disk confocal microscopy using blinking/fluctuating probes," *Nano Research* **8**, 2251-2260 (2015).
24. X. Chen, W. Zong, R. Li, Z. Zeng, J. Zhao, P. Xi, L. Chen, and Y. Sun, "Two-photon light-sheet nanoscopy by fluorescence fluctuation correlation analysis," *Nanoscale* **8**, 9982-9987 (2016).
25. T. Dertinger, A. Pallaoro, G. Braun, S. Ly, T. A. Laurence, and S. Weiss, "Advances in superresolution optical fluctuation imaging (SOFI)," *Quarterly reviews of biophysics* **46**, 210-221 (2013).
26. T. Chaigne, B. Arnal, S. Vilov, E. Bossy, and O. Katz, "Super-resolution photoacoustic imaging via flow-induced absorption fluctuations," *Optica* **4**, 1397-1404 (2017).
27. P. Dedecker, G. C. Mo, T. Dertinger, and J. Zhang, "Widely accessible method for superresolution fluorescence imaging of living systems," *Proceedings of the National Academy of Sciences* **109**, 10909-10914 (2012).
28. T. Dertinger, M. Heilemann, R. Vogel, M. Sauer, and S. Weiss, "Superresolution Optical Fluctuation Imaging with Organic Dyes," *Angewandte Chemie-International Edition* **49**, 9441-9443 (2010).
29. L. Kislely, R. Brunetti, L. J. Tauzin, B. Shuang, X. Yi, A. W. Kirkeminde, D. A. Higgins, S. Weiss, and C. F. Landes, "Characterization of porous materials by fluorescence correlation spectroscopy super-resolution optical fluctuation imaging," *ACS nano* **9**, 9158-9166 (2015).
30. S. Cho, J. Jang, C. Song, H. Lee, P. Ganesan, T.-Y. Yoon, M. W. Kim, M. C. Choi, H. Ihee, and W. Do Heo, "Simple super-resolution live-cell imaging based on diffusion-assisted Förster resonance energy transfer," *Scientific reports* **3**(2013).
31. M. Kim, C. Park, C. Rodriguez, Y. Park, and Y.-H. Cho, "Superresolution imaging with optical fluctuation using speckle patterns illumination," *Scientific reports* **5**(2015).
32. T. Dertinger, R. Colyer, R. Vogel, J. Enderlein, and S. Weiss, "Achieving increased resolution and more pixels with Superresolution Optical Fluctuation Imaging (SOFI)," *Optics express* **18**, 18875-18885 (2010).
33. X. Yi and S. Weiss, "Cusp artifact of high order Super-resolution of Optical Fluctuation Imaging," (Accompanying manuscript, submitted).
34. S. Geissbuehler, N. L. Bocchio, C. Dellagiocoma, C. Berclaz, M. Leutenegger, and T. Lasser, "Mapping molecular statistics with balanced super-resolution optical fluctuation imaging (bSOFI)," *Optical Nanoscopy* **1**, 4 (2012).
35. M. G. Kendall, *Advanced Theory Of Statistics Vol-I* (Charles Griffin: London, 1943).
36. H. Deschout, T. Lukes, A. Sharipov, D. Szigal, L. Feletti, W. Vandenberg, P. Dedecker, J. Hofkens, M. Leutenegger, and T. Lasser, "Complementarity of PALM and SOFI for super-resolution live-cell imaging of focal adhesions," *Nature communications* **7**, 13693 (2016).
37. X. Yi, "3D filaments with 100 focal plane acquisition," figshare(2017), <https://figshare.com/s/bcc1dc1080d203085e50>.
38. X. Y. Sungho Son, "live cell imaging of fluorescence protein fused  $\beta$ -Actin," figshare(2017), <https://figshare.com/s/01ee3a25ef8287063584>.
39. X. Yi, "simulation of random filaments with different conditions" figshare(2018), <https://doi.org/10.6084/m9.figshare.7033490.v1>.
40. X. Yi, "SR\_Simu3D," GitHub(2018), [https://xiyuyi.github.io/SR\\_simu3D/](https://xiyuyi.github.io/SR_simu3D/).
41. X. Yi, "SOFI2.0," GitHub(2018), <https://xiyuyi.github.io/SOFI2.0/>.
42. N. Gustafsson, S. Culley, G. Ashdown, D. M. Owen, P. M. Pereira, and R. Henriques, "Fast live-cell conventional fluorophore nanoscopy with ImageJ through super-resolution radial fluctuations," *Nature communications* **7**, 12471 (2016).
43. V. Leonov and A. N. Shiryaev, "On a method of calculation of semi-invariants," *Theory of Probability & its applications* **4**, 319-329 (1959).
44. H. Moradkhani, K. L. Hsu, H. Gupta, and S. Sorooshian, "Uncertainty assessment of hydrologic model states and parameters: Sequential data assimilation using the particle filter," *Water resources research* **41**(2005).
45. S. C. Stein, A. Huss, D. Hähnel, I. Gregor, and J. Enderlein, "Fourier interpolation stochastic optical fluctuation imaging," *Optics express* **23**, 16154-16163 (2015).
46. X. Yi, S. Weiss, "An iterative deconvolution method for fluorescence microscopy with shrinking kernel (DeconvSK)," in preparation (2018).
47. X. Yi, S. Son, R. Ando, A. Miywaki and S. Weiss, "Moments reconstruction and local dynamic range compression of high order Superresolution Optical Fluctuation Imaging," bioRxiv, DOI: <https://doi.org/10.1101/500819>